Aalborg Universitet

AALBORG UNIVERSITY
DENMARK

Neuromorphic Event-Driven Semantic Communication in Microgrids

Diao, Xiaoguang; Song, Yubo; Sahoo, Subham; Li, Yuan

Published in:
IEEE Transactions on Smart Grid

DOI (link to publication from Publisher):
10.48550/arXiv.2402.18390
10.1109/TSG.2024.3370822

Creative Commons License
CC BY 4.0

Publication date:
2024

Document Version
Accepted author manuscript, peer reviewed version

Link to publication from Aalborg University

Citation for published version (APA):
Diao, X., Song, Y., Sahoo, S., & Li, Y. (2024). Neuromorphic Event-Driven Semantic Communication in Microgrids. *IEEE Transactions on Smart Grid*, Article 10445758. Advance online publication. https://doi.org/10.48550/arXiv.2402.18390, https://doi.org/10.1109/TSG.2024.3370822

General rights
Copyright and moral rights for the publications made accessible in the public portal are retained by the authors and/or other copyright owners and it is a condition of accessing publications that users recognise and abide by the legal requirements associated with these rights.

- Users may download and print one copy of any publication from the public portal for the purpose of private study or research.
- You may not further distribute the material or use it for any profit-making activity or commercial gain
- You may freely distribute the URL identifying the publication in the public portal -

Take down policy
If you believe that this document breaches copyright please contact us at vbn@aub.aau.dk providing details, and we will remove access to the work immediately and investigate your claim.

Downloaded from vbn.aau.dk on: May 29, 2024

Neuromorphic Event-Driven Semantic Communication in Microgrids

Xiaoguang Diao, *Student Member, IEEE*, Yubo Song, *Member, IEEE*, Subham Sahoo, *Senior Member, IEEE* and Yuan Li, *Student Member, IEEE*

***Abstract*—Synergies between advanced communications, computing and artificial intelligence are unraveling new directions of coordinated operation and resiliency in microgrids. On one hand, coordination among sources is facilitated by distributed, privacy-minded processing at multiple locations, whereas on the other hand, it also creates exogenous data arrival paths for adversaries that can lead to cyber-physical attacks amongst other reliability issues in the communication layer. This long-standing problem necessitates new intrinsic ways of exchanging information between converters through power lines to optimize the system's control performance. Going beyond the existing power and data co-transfer technologies that are limited by efficiency and scalability concerns, this paper proposes neuromorphic learning to implant communicative features using spiking neural networks (SNNs) at each node, which is trained collaboratively in an online manner simply using the power exchanges between the nodes. As opposed to the conventional neuromorphic sensors that operate with spiking signals, we employ an event-driven selective process to collect sparse data for training of SNNs. Finally, its multi-fold effectiveness and reliable performance is validated under simulation conditions with different microgrid topologies and components to establish a new direction in the sense-actuate-compute cycle for power electronic dominated grids and microgrids.**

***Index Terms*—Neuromorphic computing, microgrids, hierarchical control, spiking neural network, semantic communication.**

I. Introduction

MICROGRIDS (MGs) have demonstrated their effectiveness in integrating distributed energy sources and energy storage, such as fuel cells, distributed wind and solar generations, and microturbines with the operation both in grid-connected and islanded mode [1]. To achieve proper coordination and maximum utilization from its components, many hierarchical control strategies including primary, secondary, and tertiary controls are utilized to address short and long term objectives, ranging from system dynamics to economic optimization in the system. As reviewed in [2], primary control operates with inner control of distributed generation (DG) units by adding virtual inertia. However, the lack of access to information from other sources makes it deviate from the nominal operation point [3]. On the other hand, upon deploying a communication network for information exchange between converters, secondary controllers compensate for the errors introduced by the primary control layer and achieve coordinated objectives, such as current sharing, voltage regulation, and power sharing. Objectives can also be specially designed as multiple optimization problems in complex topology as defined in [4] and [5]. The operation cost can be minimized by optimizing the dispatch of DGs. Meanwhile, the communication structure is also developed from the centralized structure to a more resilient distributed structure. Going beyond the centralized information collection, distributed control philosophy improves the system robustness by only requiring the states of adjacent nodes for sparsity in achieving system-level convergence. To this end, hierarchical coordinated control is a unique context of MGs that is highly dependent on communication. Predictive control in the secondary level in MGs is an alternative for mitigating data dropouts and latency by providing latency compensation and modified adjacency matrix in response to electrical or communications disturbances [6]. However, communication networks still expose microgrids to specific challenges, such as random communication delays [7], cyber attacks [8], and cyber link outages [9].

Talkative Power Communication (TPC) has emerged as an innovative solution [10], [11] for co-transfer of power and information, that transmits messages through power lines by encoding and superimposing on the respective bus voltages. Various digital modulation techniques, such as amplitude-shift keying (ASK), frequency-shift keying (FSK), and phase-shift keying (PSK), are utilized for overlaying data onto a reference signal [12]. An alternative approach involves modifying the carrier during the modulation process [13]. TPC modulations can also be implemented entirely in the digital domain [14]. However in AC systems, these signals cannot traverse through transformers due to the absence of a zero-sequence path. Similarly, in DC systems, these signals are obstructed by solid-state medium frequency transformers (SSTs) as SST inherently functions as a DC-DC converter which decouples the input and output. The encoded signals can also be attenuated by the input capacitor of solid-state transformers (SSTs). This constraint restricts the application of TPC in microgrids with different voltage levels, which thereby encounters significant technical difficulties when scaling up to high voltage (HV) levels and number of converters [15]. Apart from the power inefficiency incurred by TPC, its scalability and evolution beyond the

This work is supported by the Nordic Energy Research programme via Next-uGrid project n. 117766. The authors would like to acknowledge Prof. Osvaldo Simeone for his advice and inputs in the organization of this paper.

Xiaoguang Diao is with Hubei Key Laboratory for High-efficiency Utilization of Solar Energy and Operation Control of Energy Storage System, Hubei University of Technology, Wuhan 430068, China and the Department of Energy, Aalborg University, Denmark. (e-mail: 2018202070081@whu.edu.cn)

Yubo Song, Subham Sahoo and Yuan Li are with the Department of Energy, Aalborg University, Denmark. (e-mail: {yuboso, sssa, yuanli}@energy.aau.dk)

Corresponding author: Subham Sahoo

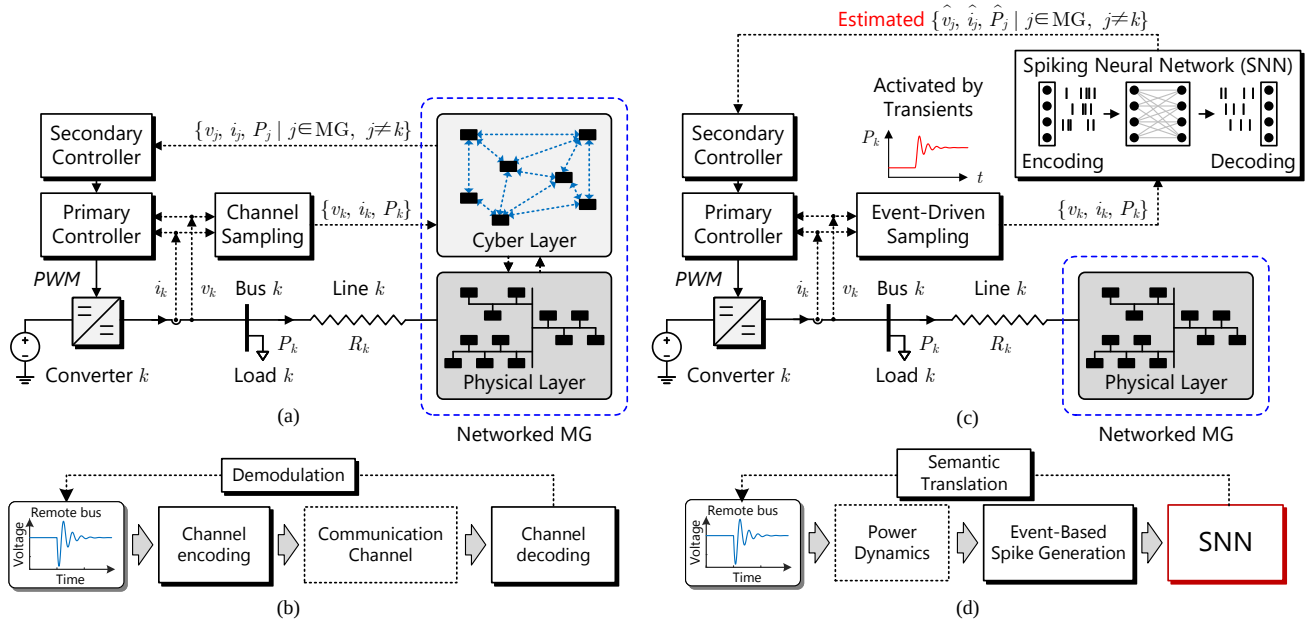

Fig. 1. Going beyond traditional communication norms to task-oriented semantic communications in microgrids: (a) conventional cyber-physical control framework, (b) stages in traditional communication, (c) proposed NSC-based coordinated control framework, (d) simplified and reduced stages in NSC.

request-receive communication protocol still remain a big question in MGs. This sets up the foundation for innovations in new co-transfer technologies beyond the state-of-the-art.

In this regard, the development of artificial intelligence (AI) has opened up unconventional possibilities to go beyond traditional model-driven norms. AI-based semantic communication is able to solve the specific challenges of communication in MGs by eliminating key stages, such as signal modulation and communication channels. Basically, *semantic communication* is a task-oriented approach that does not rely on bit sequences and allows for the exchange of most significant information through various forms of transmission [16]. This extends an astonishing opportunity for the power systems communication paradigm, as electrical transients inherently contain valuable information of system dynamics. As a result, the power flows among the lines is hypothesized to be sufficient to distill coordination among different converters in MG. However, a critical requirement is a robust decoder/processor that can effectively *translate* the global communicative signatures from the transients. Although the hierarchical evolution using AI in distributed optimization tasks, particularly for secondary control applications [17] has been a promising alternative for MGs, it is essential to exercise caution considering high energy requirements, low efficiency, latency and implementation complexity of many neural network (NN) architectures.

Inspired by the function of biological brains, we explore by showcasing in DC microgrids the potential of *neuromorphic* processors, which exploit Spiking Neural Networks (SNNs) as a low-energy decoder for converters to communicate between each other only using the non-modulated power flows between them. Unlike the next generation artificial neural networks (ANN), which always utilizes real valued samples for learning and inferences, SNN simply compute using binary spikes to excite a change in its corresponding weights by governing local dynamics [18]. As a result, SNN can be trained online in a sparse manner corresponding to any physical disturbances only using local power flow measurements. Consequently, the proposed inferential mechanism in this paper operates on an entirely different protocol, namely the *publish-subscribe* architecture [19]. From an application perspective, dedicated spike-based processors, such as Intel's *Loihi* 2 and IBM's *TrueNorth* offers several advantages:

- *High energy efficiency*: Since most neurons in a SNN remain idle in the absence of *events*, the spike activity is sparse. This sparsity leads to energy-efficient computations as processing binary spikes `1` and `0`, requiring less computational energy compared to the complex operations involving high-precision floating-point numbers used in ANNs [20].
- *Low latency*: Considering the control application of MGs in this paper, the overall delay of transmitting information packets from one end to another is significantly reduced not only due to information embedding on instantaneous power but also due to the low latency of SNNs itself.
- *Hardware performance*: Neuromorphic technology is designed with an asynchronous address event representation (AER) architecture, which differs from the rest that still rely on a global clock. This AER architecture aligns well with the asynchronous operation of SNN, enabling low-latency and energy-efficient behavior [21], [22].

In the recent literature, SNNs have demonstrated successful applications in image classification [23] and wireless communications [24] only using spikes generated from a physical channel/medium to extract contextual information or messages. However, its synthesis process including decoding the spikes to meaningful real-valued information is carried out by powerful neuromorphic sensors in those applications. On the other hand, augmentation of a new spiking-based sensing technology is not a straight-forward mechanism for power systems today, since their operations are only equipped to

translate and operate with real-valued measurements.

This is where we propose an elementary method to generate spikes based on *semantic events* [25], [26] collected from the existing measurements in microgrids that consequently federates the training of SNN at each node. By doing so, not only the energy consumption can be significantly reduced by collecting binary data instead of floating point numbers, but it will also expedite low-power edge processors. This online training is triggered only when nodal power dynamics exceed a pre-defined event-detection threshold. Finally, these events are encoded and decoded as spikes for remote estimation. As a result, the neuromorphic semantic communication (NSC) allows us to go beyond the current cyber-physical architecture of microgrids (as shown in Fig. 1(a) and (b)) to a novel intrinsic communication principle (as shown in Fig. 1(c) and (d)) for power electronic converters only using the power flows between them. The comparison of NSC, TPC and traditional cyber layer communication (CLC) are presented in Table I.

To sum up, the research contributions of this paper are:

1) A pioneering application of neuromorphic computing in the coordinated control of MGs is proposed. To ensure its suitability for coordinated control of microgrids and prospective extension in larger systems, this paper tailors spiking neural networks (SNNs) as a grid-edge inference technology with detailed steps of implementation. By eliminating the communication infrastructure, the proposed philosophy not only removes exogeneous arrival paths for cyber-attackers and other reliability issues in the cyber layer, but also unravels unification of power and information in general using the *publish-subscribe* protocol that can be extended for many applications.
2) Since SNNs operate using the energy-efficient binary spikes in a sparse and online fashion using spike timing dependent plasticity (STDP), we employ *semantic events* translating the dynamic response of each converters with respect to the measured power flows as spikes to carry out online training of NSC.
3) Going beyond TPC that allows co-transfer of power and data but are limited by electrically isolated stages, the proposed communication principle is not limited by such stages that physically block the zero-sequence path. Its scalability and flexibility for different voltage levels and system topologies has been investigated in detail. Moreover, it also promises high computational energy efficiency during data processing and learning, that has been bench-marked with respect to binary-activated recurrent neural networks (RNNs) and ANN.

In this paper, DC MGs have been focused to showcase the principle behind the proposed NSC, whereas it is also potentially applicable to AC systems where the data collection methodology may need to be revised.

II. Neuromorphic Coordinated Control of Microgrids

A. Problem formulation and motivation

The conventional cyber-physical framework of the most reliable infrastructure, i.e., distributed coordination in a DC MG is depicted in Fig. 1(a). In this framework, each converter is locally regulated by the primary controller and globally by the secondary controller that relies on exchange of real-time information, including voltage v_j and current i_j from the neighboring nodes $j \in N_k$ in Fig. 1(a), where N_k denote the set of neighbors for converter k. It is crucial to note that the stability and reliability of MGs heavily rely on the effectiveness of the communication network [8], [27]. However, as presented in Fig. 1(b), the conventional communication methods/protocols in MGs include stages such as, modulation, transmission, and demodulation, which is done in a timely process that introduces the notion of bandwidth and consequently suffers from communication delays [7], cyberattack vulnerability [8], and susceptibility to cyber link outages [9]. These disturbances can range from few milliseconds to seconds and can negatively impact the dynamic performance and stability of MGs. Although co-transfer technologies such as TPC can eliminate the need for conventional communication infrastructure, it is still susceptible to scalability in high voltage levels (due to mutual inductance between lines causing signal interference) and path blockage beyond galvanic isolation, which can affect communication reliability. As a result, new intrinsic and scalable means of communication among converters is needed to overcome the said challenges and investigate the ongoing digitalization measures in MGs.

This section unravels a novel end-to-end NSC-based coordinated control framework, as depicted in Fig. 1(c), which comprises of the SNN as its key component. Its protocol stages are illustrated in Fig. 1(d), where instead of transferring information from one end to the other, remote information can be inferred at each end using the spatio-temporal pattern of the power dynamics corresponding to the physical disturbances. Using event-driven sampling, *meaningful* information is filtered and encoded into spikes for initial weight determination of SNN to be deployed at each bus. Relying on the *publish-subscribe* architecture [19] depending on a global update that can be translated as any disturbance in MGs, SNNs then infer the information of remote buses by measuring power flows. It is worth mentioning that the spike timing dependent plasticity (STDP) feature further allows online training of SNNs only by measuring power flows to adapt its weights accordingly.

As the proposed framework is significantly different from the traditional cyber-physical arrangements (in Fig. 1(a)), we firstly discuss the hierarchical control using conventional communication architecture and then discuss the specific design and implementation steps for integrating neuromorphic based semantic coordination into the control of MGs. Building upon this research in end-to-end low power NSC for MGs, this paper draws inspiration and adapts the proposed communication policy only using power flows as the communication channel

TABLE I
Comparative Evaluation of NSC, TPC and CLC.

Methods	Prone to Delay?	Prone to Cyberattack?	Prone to Channel outage?	Prone to Inefficiency?
CLC [7], [8]	Yes	Yes	Yes	No
TPC [10], [11]	No	No	No	Yes
NSC	No	No	No	No

for coordinated control of MGs, as shown in Fig. 1(c) and (d).

B. Conventional hierarchical control in MGs

Fig. 1(a) depicts the conventional hierarchical control structure of a DC MG. The primary control uses local measurements to regulate the output voltage based on a $V-I$ droop control strategy. Additionally, the local sampling data is shared with adjacent nodes through the cyber layer, facilitating coordination and monitoring.

1) Primary control: The primary control layer in converter k is implemented as:

$$v_{ref,\,k}(t) = v_k(t) - m_k i_k(t) \tag{1}$$

where, m_k is the droop gain, which is calculated using $\Delta V_k / I_{k_{max}}$ with ΔV_k and $I_{k_{max}}$ being the maximum voltage deviation and maximum output current of converter k, respectively. Furthermore, i_k and $v_{ref,k}$ denote the converter output current and voltage reference of converter k, respectively.

2) Distributed secondary control: The secondary controller plays a crucial role in achieving voltage regulation and other energy management schemes. As distributed secondary control offers highly reliable and cost-efficient coordination [1], we consider it as the best candidate for CLC in this paper. With distributed secondary control, the local voltage set point can be expressed as:

$$v_k^*(t) = v_{ref,\,k}(t) + \delta v_k^{\mathrm{I}}(t) + \delta v_k^{\mathrm{II}}(t) \tag{2}$$

where, $v_{ref,\,k}$ is the voltage regulation term generated by the primary controller in (1). The first voltage correction term δv_k^{I} is generated by the voltage observer and further compensated by the secondary PI controller:

$$\bar{v}_k(t) = v_k(t) + \int_0^t \sum_{j\in N_k} a_{kj}(\bar{v}_j(t) - \bar{v}_k(t))\mathrm{d}\tau \tag{3a}$$

$$\delta v_k^{\mathrm{I}}(t) = k_{pU}(v_{ref} - \bar{v}_k(t)) + k_{iU}\int_0^t (v_{ref} - \bar{v}_k(t))\mathrm{d}\tau \tag{3b}$$

where, $\bar{v}_k(t)$ is the average voltage observed at bus k, N_k is the set of nodes that are adjacent to node k in the cyber graph. In a graph with N nodes, each node represent a converter, that are communicating among each other using edges through an associated adjacency matrix, $\mathbf{A}_{\mathrm{G}} = [a_{kj}] \in R^{N\times N}$, where the communication weight (represented by a_{kj}, i.e., from node j to node k) is formulated as: $a_{kj} > 0$, if $(\psi_k, \psi_j) \in \mathbf{E}$, where $\mathbf{E}$ represents an edge connecting two different nodes, with ψ_k and ψ_j representing a local node and its neighboring node, respectively. If the cyber link connecting ψ_k and ψ_j is absent, a_{kj} = 0. More modeling preliminaries of the cyber graph can be obtained from [28]. Furthermore, the second voltage correction term δv_k^{II} is generated by cooperative regulators for particular objectives. For current sharing, the regulation term is calculated by:

$$\lambda_k(t) = \sum_{j\in N_i} a_{kj}(i_j(t) - i_k(t)) \tag{4a}$$

$$\delta v_k^{\mathrm{II}}(t) = k_{pI}\lambda_k(t) + k_{iI}\int_0^t \lambda_k(t)\mathrm{d}\tau \tag{4b}$$

Similarly, for power sharing objective, the regulation term is:

$$\eta_k(t) = \sum_{j\in N_i} a_{kj}(P_j(t) - P_k(t)) \tag{5a}$$

$$\delta v_k^{\mathrm{II}}(t) = k_{pP}\eta_k(t) + k_{iP}\int_0^t \eta_k(t)\mathrm{d}\tau \tag{5b}$$

where, k_{pI}, k_{iI}, k_{pP}, and k_{iP} are the proportional and integral coefficients of PI controllers for current sharing and power sharing, respectively.

Given that the physical layer of the MG and cascaded control structure from the primary control loop to the PWM stage remain the same in both Fig. 1(a) and (c), the key distinction of incorporating NSC instead of relying on the traditional CLC lies in how the dynamic measurements from the remote nodes are efficiently predicted to disregard any exogenous arrival paths or unreliable cyber scenarios, which is the main contribution of this paper. In addition to the elimination of a dedicated communication channel that primarily relies on the *request-receive* protocol, we leverage the proposed NSC framework to infer real-time information using power flows by deploying SNN at each bus. We firstly cover the background of the biological neuron modeling for SNNs and then discuss the offline initial weight determination of SNN at each bus in the upcoming subsections.

C. Fundamentals of SNN operation

Instead of the summation functions in multilayer perceptron networks for ANN, SNN employs neuronal dynamics that rely on the integration process with a framework that triggers action potential only above a critical voltage [29]. As shown in Fig. 2(b), a biological neuron is basically excited by a current $I(t)$ as a pulse input coming from the nearby neurons into the axon of the cell body. Similar to the electrical properties in a RC circuit (see Fig. 2(a)) with a cell voltage V_r, the current $I(t)$ will only flow given that the capacitor voltage V_{th} is more than V_r. Mathematically, this can be represented by:

$$I(t) = \frac{V_{th}(t) - V_r}{R} + C\frac{\mathrm{d}V_{th}}{\mathrm{d}t} \tag{6}$$

Considering the time constant τ_m = RC as the *leaky integrator*, we get:

$$\tau_m \frac{\mathrm{d}V_{th}}{\mathrm{d}t} = -[V_{th}(t) - V_r] + RI(t) \tag{7}$$

Translating the electrical specifications into the neuron cell, we can then refer V_{th} to be the membrane potential and τ_m to be the membrane time constant of the neuron. Due to the notion of leakage of charge with a time constant τ_m and (7), this neuron model is commonly called as the leaky-fire and integrate (LIF) model. Approximating the LIF neuron dynamics in Fig. 2(b) using the Euler method [29], we get:

$$\tau_m \frac{\mathrm{d}V_{mem}}{\mathrm{d}t} = -(V_{mem} - V_{th}) + \frac{I_s}{g} \tag{8}$$

where, V_{mem} is the membrane potential, g is the leaky conductance, V_{th} is the threshold, I_s is the synaptic current and τ_m is the membrane time constant.

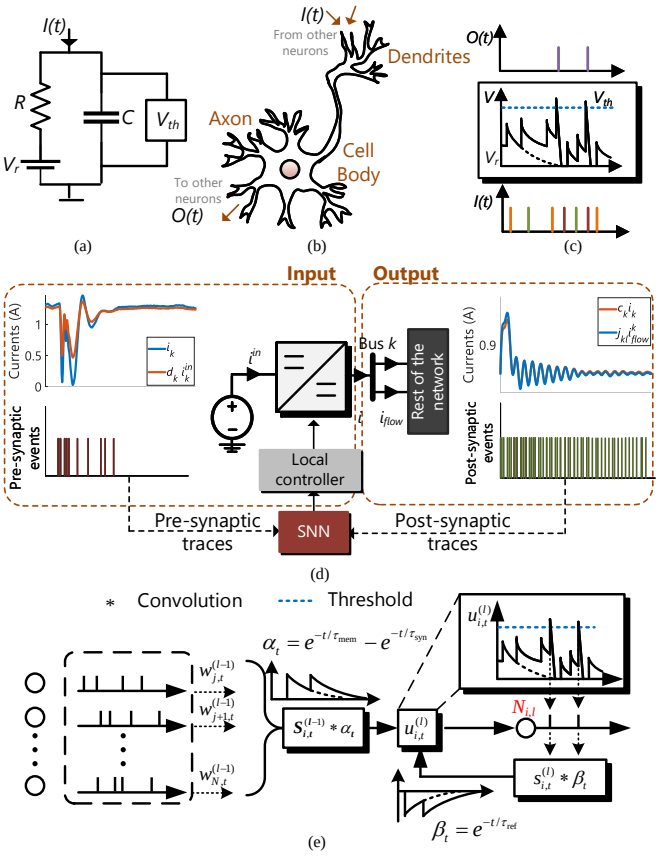

Fig. 2. Initial weight determination of SNN at bus k – Pictorial depiction of a (b) RC circuit and its structural duality with (b) biological neuron, where the input current $I(t)$ acts as an excitation signal into both the circuit and the neuron – its excitation dynamics are then translated into *meaningful* output spikes for the learning of NSC using a (c) voltage threshold V_{th} based criteria, (d) Similar to the biological neurons in (b), a converter having disturbances in its input and output can consequently correspond to pre-synaptic and post-synaptic events, respectively, (e) Information-theoretic learning based communication using spiking neural networks (SNNs) and the spike response model (SRM) for simulation of a LIF neuron.

Considering the dynamics in (8) and selection of a corresponding event-triggering criteria [30], the input spikes can then be determined corresponding to rising or falling edges in $I(t)$. As shown in Fig. 2(c), the input spikes that manage to invoke beyond the membrane potential V_{th} result into a selective number of output spikes.

Extending the single neuron structure to a bidirectional DC/DC converter in Fig. 2(d), the current excitation can either emanate from the input, such as intermittent generation from renewable energy sources, or the output, such as load change or tie-line outage. Since the current flow is in both directions as compared to the case in Fig. 2(b), we decipher both input as well as output dynamics to achieve accuracy in the estimation of information at remote buses. Using multiple data set-points corresponding to different operational scenarios, semantic data collection is performed to assign the initial weights of SNN, which will be discussed later.

D. Network model of SNN

Before discussing the weight initialization strategy for SNNs to be deployed at each bus, we firstly uncover the underlying theory behind the entire network to be modeled. The neuron model in Fig. 2(e) is the spike response model (SRM). It is a widely recognized model that effectively represents the characteristics of biological neurons while retaining simplicity, which makes it well-suited for the intended application of the NSC-based coordinated control framework in MGs [24].

In Fig. 2(e), the neuron $N_{i,l}$ is connected with its preceding neurons by different synaptic weights $\{w_{j,l-1} \| \ j \in \text{Layer}\,(l-1)\}$. The preceding neurons can transmit binary spikes to $N_{i,l}$. The membrane potential $u_{i,l}$ of $N_{i,l}$ represents an analog state to describe the contribution of the spikes. When $N_{i,l}$ receives a spike, $u_{i,l}$ momentarily increases and decays exponentially over time. This behavior is described as the second-order synaptic filter, $\alpha_t = e^{-t/\tau_m} - e^{-t/\tau_{syn}}$. Referring to (8), the decay process is modeled as the first-order feedback filter $\beta = -e^{-t/\tau_{ref}}$ with finite positive constants $\tau_m, \tau_{syn}, \tau_{ref}$. The membrane potential $u_{i,l}$ is computed as the sum of the filtered contributions from incoming spikes and the neuron's own past outputs as follows:

$$u_{i,t}^{(l)} = \sum_{j=1}^{N} w_j^{(l-1)} \cdot (\alpha_t * s_{j,t}^{(l-1)}) + \beta_t * s_{i,t}^{(l)} \tag{9}$$

where, $*$ denotes the convolution operator, and $s_{j,t}^{(l-1)}$ represents the spike from layer $(l-1)$. The spike $s_{i,t}^{(l)}$ is generated by neuron $N_{i,l}$ at time step t when its membrane potential $u_{i,l}^{(l)}$ surpasses the threshold U_{thr}, using:

$$s_{i,t}^{(l)} = H(u_{i,t}^{(l)} - U_{thr}) \tag{10}$$

where, $H(\cdot)$ is the Heaviside step function, given by:

$$H(x) = \begin{cases} 1 & x > 0 \\ 0 & x \leq 0 \end{cases} \tag{11}$$

Remark I: *Unmodulated power flows with pub-sub communication protocol inherently imbibe communicative features due to the spatio-temporal patterns of voltage V in power electronic grids, where $V = V_0 e^{-a}$ such that $a = \{t, x\}$ corresponding to time and space, respectively. As SNNs are highly capable of synthesizing these spatio-temporal patterns in an energy-efficient and online fashion, we underline our proposal with SNN as an energy-efficient grid-edge intelligence tool for coordination and health monitoring of future power systems.*

E. Data collection and offline design of SNN

It is worth notifying that *events* in this paper denote the physical disturbances in the system. Such disturbances either in the input or output of DC/DC converter in Fig. 2(d) are essentially formalized by the power dynamics turned events locally at each bus with the power lines being the propagating medium itself. Hence, the input dynamics in Fig. 2(d) of DC/DC converter k associated with the capacitor current i_k^C and inductor voltage v_k^L can be given by:

$$\begin{cases} i_k^C(t) = C_k \frac{\mathrm{d}v_k}{\mathrm{d}t} = i_k(t) - d_k i_k^{in}(t) \\ v_k^L(t) = L_k \frac{\mathrm{d}i_k}{\mathrm{d}t} = v_k(t) - d_k v_k^{in}(t) \end{cases} \tag{12}$$

where, d_k denotes the voltage amplification ratio between the input and output end of DC/DC converter k, i_k^{in} and v_k^{in} denote

the input current and voltage of converter k, respectively. Moreover, L_k and C_k denote the inductor and capacitor in the DC/DC converter k, respectively. Finally, the corresponding error signals for both currents and voltages to formalize/trigger the input events in k^{th} converter (see Fig. 2(d)) are given by:

$$\begin{cases} \Omega_i(t) = v_k^L(t) - e_k^i(t) \\ \Omega_v(t) = i_k^C(t) - e_k^v(t) \end{cases} \tag{13}$$

where, $e_k^i(t) = i_{ref,k}^{in}(t) - i_k^{in}(t)$ and $e_k^v(t) = v_{ref,k}(t) - v_k(t)$. Since the error values e_k^V and e_k^i have a low time constant with respect to the given switching frequency as compared to the ones using CLC, the physical system semantics is used to extrapolate the most significant data to be collected for each converter. Not only this data collection principle allow collection of qualitative data, it ensures the most significant information to be distilled for effective training of the provisional SNN.

To scale from the local to global events, remote estimation using the output dynamics of all the converters in Fig. 2(d) can be further distilled into a vector representation:

$$\mathbf{C}\dot{\mathbf{V}}(t) = \mathbf{J}\mathbf{I}_{\mathbf{flow}}(t) - \mathbf{di}^{\mathbf{in}}(t) \tag{14}$$

where, $\mathbf{J}$ is a row matrix with binary values, such that j_{kl} will be 1 only if there is a direct physical connection between converter k and l, or otherwise. Moreover, $\mathbf{I_{flow}}$ is a column matrix that comprises the tie-line flow currents into the connected lines resulting out of the output current i_k, such that $i_k = \sum i_{flow}$. Furthermore, $\mathbf{C}, \mathbf{V}, \mathbf{d}$ and $\mathbf{i^{in}}$ denote $k \times k$ diagonal matrices for C_k, v_k, d_k and i_k^{in}. The formalization of output events can then be carried out using:

$$\Omega_o(t) = C_k \dot{v}_k(t) - \dot{I}_{flow}^k(t) \tag{15}$$

Using the spatio-temporal pattern exploration hypothesis in Remark I, for a given network admittance matrix, each output current has a given distribution of intrinsic communication signatures in the form of i_{flow}, that can be estimated using the following data collection process. Finally, sparse sampling and data collection is formalized only the semantic event detection criteria in (13) and (15) exceed a given threshold:

$$||\Omega_v(t)|| > \sigma_{th}^V, \quad ||\Omega_i(t)|| > \sigma_{th}^I, \quad ||\Omega_o(t)|| > \sigma_{th}^o \tag{16}$$

where, σ_{th}^V, σ_{th}^I are the thresholds for input events in (13) and σ_{th}^o denote the threshold for the output event in (15), respectively. To achieve good resiliency against noise, a state-dependent threshold can be used [31].

The input events are then translated into spikes using `Algorithm 1` such that SNN exploits the local measurements and their dynamics to estimate remote measurements. The output spikes can also be generated by following `Algorithm 1` for the dynamics in (14) and triggering criteria in (15). Finally using the NSC-based control method, the remote voltage and current in (3a), (4a) and (5a) are replaced with the estimated values $\hat{\circ}$, as follows:

$$\bar{v}_k(t) = v_k(t) + \int_0^t \sum_{j \in N_{flow}} (\hat{\bar{v}}_j(\tau) - \bar{v}_k(\tau)) \mathrm{d}\tau \tag{17a}$$

$$\lambda_k(t) = \sum_{j \in N_{flow}} (\hat{i}_j(t) - i_k(t)) \tag{17b}$$

$$\eta_k(t) = \sum_{j \in N_{flow}} (\hat{P}_j(t) - P_k(t)) \tag{17c}$$

where, $\hat{P}_j(t)$ is obtained by $\hat{P}_j(t) = \hat{i}_j(t)\hat{v}_j(t)$ and N_{flow} is the set of nodes that are adjacent to converter k in the physical tie-line admittance network graph. Having discussed the offline preliminary design of SNN at each node, we now discuss its online training based on the spike timing dependent plasticity (STDP) feature in the next section.

Algorithm 1 Input event translation to spikes.

Input: m^{th} sample of voltage $v[m]$, current $i[m]$
Thresholds of voltage and current variance to trigger and hold an event σ_{th}^V, σ_{th}^I

$V^{ben}[0] \leftarrow 0$, $I^{ben}[0] \leftarrow 0$
Verify Ω_v and Ω_i using (16)
if Ω_v `OR` Ω_i **then**
  `event`$[m]$ starts
  repeat
    SNN is activated
    // Update the benchmarks
    Update $V_{ben}[m]$: V_{ben}=1
    Update $I_{ben}[m]$: I_{ben}=1
    $m \leftarrow m + 1$
    Re-verify Ω_v and Ω_i by Eq. (16)
  until `NOT` $(\Omega_v$ `OR` $\Omega_i)$
  `event`$[M]$ ends
  Hold $V_{ben}[M]$ and $I_{ben}[M]$ as the steady-state values

III. Spike Timing Dependent Plasticity

A. Online weight adaptation of SNN

After obtaining the preliminary offline design of SNN, the dynamic weight adaptation corresponding to different transients/events is carried out using *Spike timing dependent plasticity* (STDP) [32]. STDP is a neurobiological concept that describes how the strength of a synapse in Fig. 2(b), which is the connection between two neurons, can be modified based on the precise timing of the spikes from inputs and outputs or the action potentials in these neurons. It is a fundamental mechanism that underlies learning and memory in the brain, which makes it a biology-plausible training method and allows online adaptation of the weights of SNN. The mathematical formulation behind the STDP based weight update policy is as follows:

$$\Delta W = \begin{cases} A_+ e^{(t_{pre} - t_{post})/\tau_+} & (t_{post} > t_{pre}) \\ -A_- e^{-(t_{pre} - t_{post})/\tau_-} & (t_{post} < t_{pre}) \end{cases} \tag{18}$$

where, ΔW denotes the change in the synaptic weight of SNN, A_+ and A_- determine the maximum amount of synaptic modification (which occurs when the timing difference between pre-synaptic and post-synaptic spikes in Fig. 2(d) is close to zero), τ_+ and τ_- determine the ranges of pre-to-postsynaptic inter-spike intervals over which synaptic strengthening or weakening occurs. As illustrated in Fig. 3(a), t_{pre} and t_{post} are the timings of the pre-synaptic and post-synaptic

spikes, that correspond to the input and output disturbances of the DC/DC converter in Fig. 3(b), respectively. As illustrated in Fig. 3(a), if the postsynaptic neuron spikes arrive after the pre-synaptic neuron, $\Delta W > 0$, or otherwise, $\Delta W < 0$. The weight update policy and its biological plausibility is explained by the Hebbian Principle, that is often summarized as "neurons that fire together wire together". If a pre-synaptic neuron fires just before a postsynaptic neuron, the connection between them is strengthened, often known as long-term potentiation (LTP) of the synapse [33]. Otherwise, the connection is weakened, often known as long-term depression (LTD) of the same synapse.

Based on the abovementioned definitions, it is vital to analyze the time difference between the pre-synaptic and post-synaptic spikes, given by:

$$\Delta t = t_{pre} - t_{post} \tag{19}$$

From a DC/DC converter perspective, this would imply that the time difference Δt could either arise depending on the physical disturbances that is either in the input or output stage, as illustrated in Fig. 3(b).

B. Calculation of $\sum_{i=1}^{Z} e^{\Delta t_i}$ and $\sum_{i=1}^{Z} e^{-\Delta t_i}$

Keeping track of the pre-and postsynaptic spikes for the number of neurons from 1 to Z, a neuron will receive numerous pre-synaptic spike inputs that needs to be processed simultaneously by the SNN. The post-synaptic neuron can be defined by:

$$\tau_{-}\frac{\mathrm{d}L}{\mathrm{d}t} = -Q \tag{20}$$

and for every postsynaptic neuron spikes, it is updated using:

$$Q(t) = Q(t) - A_{-} \tag{21}$$

In this manner, $Q(t)$ tracks the number of postsynaptic spikes over the given timescale τ_{-}. Similarly, for each pre-synaptic neuron, we define:

$$\tau_{+}\frac{\mathrm{d}R}{\mathrm{d}t} = -S \tag{22}$$

and for every spike on the pre-synaptic neuron, it is updated using:

$$S(t) = S(t) + A_{+} \tag{23}$$

It is worth notifying that the variables $Q(t)$ and $S(t)$ are quite similar to the notion of synaptic conductance $g(t)$ in (8), except that they are particularly defined for spike timings on a much longer timescale. Based on the illustration of ΔW in Fig. 3(a), $S(t)$ is inherently negative that is used to induce LTD ($\sum_{i=1}^{N} e^{-\Delta t_i}$) and $Q(t)$ is always positive used to induce LTP ($\sum_{i=1}^{N} e^{\Delta t_i}$). The reason behind the negative and positive signs of $S(t)$ and $Q(t)$ are because they are updated by A_{-} and A_{+}, respectively. As illustrated in Fig. 3(b), the weight increment/decrement at t_{pre} and t_{post} can be given by:

$$\Delta W(t_{pre}) = S(t_{pre})W(t_{pre}) \tag{24}$$

$$\Delta W(t_{post}) = Q(t_{post})W(t_{post}) \tag{25}$$

To implement STDP in SNN, based on the pre-synaptic and post-synaptic timing, update of the variables $Q(t)$ and $S(t)$ vary their synaptic conductance. With the peak synaptic conductance g_i for a synapse i bounded between [0, g_{max}], it is modified accordingly based on either LTP or LTD condition using:

$$\bar{g}_i = \begin{cases} \bar{g}_i + Q(t)\bar{g}_{max} \ \textit{if} \ \textbf{LTP} \\ \bar{g}_i + S(t)\bar{g}_{max} \ \textit{else} \end{cases} \tag{26}$$

Its update corresponding to the LTD or LTP conditions in Fig. 3(b) can be seen in Fig. 3(c), that is used to update the synaptic conductances of the SNN allowing online adaptation corresponding to any transient in the local measurements. As illustrated in Fig. 3(c), the total excitatory synaptic conductance $g_E(t)$ for Z pre-synaptic neurons is given by:

$$g_E(t) = \sum_{i=1}^{Z} g_i(t) \tag{27}$$

In this way, the online weight update policy subject to selective spikes update the SNN network weights for every physical disturbance in the MG.

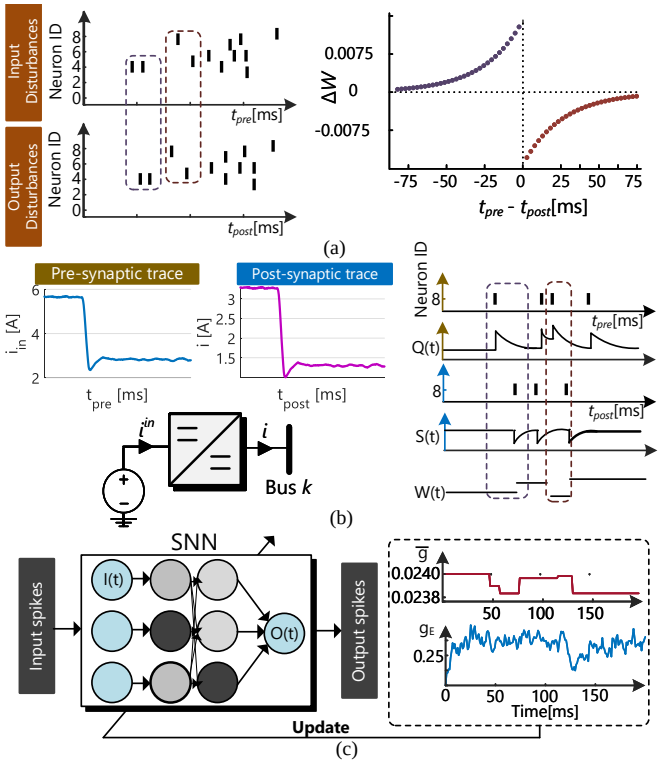

Fig. 3. Online weight update policy of SNN based on the spike-dependent timing plasticity (STDP): (a) Long-term potentiation (LTP) and depression (LTD) based on the excitation of the disturbance observed initially either in the input or the output of the DC/DC converter leading to the trajectory of weight update as per (18), (b) Update of the variables $Q(t)$ and $S(t)$ to formalize the SNN weights as per (24)-(25), (c) update of the synaptic conductance g_i (neuronal) and g_E (total) corresponding to the LTP and LTD events.

C. Design of SNN for MGs

To optimize the application of SNN in control for MGs, it is necessary to tailor the design of the SNN specifically for this purpose.

To capture the non-linear dynamics accurately, the derivatives of the typical measurements, bus voltages and output currents of each converter are considered as inputs for their respective SNN. To enhance SNN performance, we employ an input layer of 256 neurons. This allows for a more comprehensive representation of the input signals and facilitates the extraction of relevant features. The number of neurons in the output layer depends on the number of output signals required. In this study, each source needs to receive remote voltage and current information of the remaining buses. For instance, in a three-bus system in a symmetric ring topology, each source requires voltage and current data from the rest of the two sources. For an asymmetric radial topology, the number of inputs will vary based on the physical admittance matrix corresponding to each bus. This means that the SNN should have at least 4 output neurons to provide this information. The number of hidden layers and neurons in each hidden layer has been selected after adjudging a significant balance between accuracy and efficiency. The parameters used for designing SNNs in this paper can be found in Appendix.

IV. Results and Discussions

A. Simulation results

To assess the effectiveness and versatility of the proposed NSC-based coordinated control across various voltage levels, topologies, control objectives, and its robustness against the SST and line outages, we consider four test cases (shown in Fig. 4) and an IEEE 14 bus system in MATLAB/Simulink environment. The training process was carried out using Python, and the model was saved for integration into Simulink for implementation of NSC based control. The description of each disturbance has been categorized into time windows, also termed as "stages", can be found in Table II. The system parameters specific to each scenario, starting from Case I to Case V, are provided in Table III. For all the case studies, it should be noted that estimated values from SNN are depicted as $\hat{\circ}$, whereas the measured values as $\circ$ for voltage, current and power. For simplicity, the dataset only includes disturbances, such as load step changes and line outages for a preliminary investigation of secondary controller. More dynamic disturbances will be considered as a future scope of work to investigate the sensitivity and stability of its performance using a high-performance SNN.

TABLE II
Description of the Stages in Simulation Studies.

Cases	Stage I ($t_{1\text{-}2}$)	Stage II ($t_{2\text{-}3}$)	Stage III ($t_{3\text{-}4}$)	Stage IV (t_4-end)
Case I	Load increase	Load decrease	Line outage	–
Case II	Load increase	Line outage	Line outage	Load decrease
Case III	Load increase	Load decrease	Line outage	–
Case IV	Load increase	Load decrease	Line outage	Load decrease
Case V	PV power decrease	PV power increase	Load decrease	–

1) Case I: Two-Bus DC microgrid: The secondary control objective of Case I is proportionate current sharing. At time t_1 in Fig. 5(a), a step increase in the load from 64 W to 160 W occurs in stage I. As a result of NSC-based coordinated control, i_1 and i_2 rise simultaneously and reach the same steady value, thereby fulfilling the secondary control objective. This is made possible by the NSC-based coordinated control in (17b) that provides the estimated values $\hat{i}_2$ and $\hat{v}_2$ after decoding from SNN during dynamic processes shown in Fig. 5(b). Furthermore, v_1 decreases due to the $V-I$ droop control described in (1), while v_2 increases to provide additional power from converter II for current sharing. Similarly at the instant t_2, when the system load decreases to 64 W, both i_1 and i_2 decrease together and reach the same steady value, confirming the effectiveness of the current sharing control.

TABLE III
System Parameters of different Simulation cases.

	Parameter	Symbol	Specification
Case I	Rated voltage	V_n	48 V
	Rated power	P_1=P_2	300 W
	Line resistance	R_{12}	1.5 Ω
	Line inductance	L_{12}	50 µH
Case II	Rated voltage	V_n	400 V
	Rated power	P_1=P_2=P_3	10 kW
	Line resistance	R_1, R_2, R_3	1.5 Ω, 1.8 Ω, 2 Ω
	Line inductance	L_1, L_2, L_3	50 µH, 60 µH, 66 µH
Case III	Rated voltage	V_n	48 V/400 V
	Rated power	P_1=P_2	10 kW
	Line resistance	R_{12}	3 Ω
	Line inductance	L_{12}	1.5 mH
Case IV	Rated voltage	V_n	400 V
	Rated power	P_1=P_2=P_3	10 kW
	Line resistance	R_1, R_2, R_3	2.4 Ω, 1.2 Ω, 2.8 Ω
	Line inductance	L_1, L_2, L_3	1 mH, 0.5 mH, 0.75 mH
Case V	Rated voltage	V_n	400 V
	Rated power	P_1=P_2=P_3	15 kW
	ES voltage	$V_{\text{ES1-4}}$	96 V
	MPPT voltage	V_{MPPT}	245.6 V

At time t_3 (stage III), a line outage occurs between the converters, resulting in islanded operation of both converters. Consequently, the entire secondary control loop, including the SNN represented by the dotted lines, becomes inactive.

In Fig. 5(c), we present the spikes corresponding to N = 256 neurons between the output layer and the hidden layer during the time interval [1, 1.4] s. As depicted in Fig. 5(a) and (b), during [1, 1.2] s, the currents and voltages undergo dynamic changes, and after 1.2 s, their variations become less pronounced. Accordingly, the spikes in Fig. 5(c) also exhibit more dynamic behavior during the initial phase and become relatively stable as the steady state is reached.

The spikes from various neurons are depicted in Fig. 5(d), generated in correspondence with the events obtained using (16) illustrated in Fig. 5(c). The computational energy consumption, shown in Fig. 5(e), dynamically changes in tandem with the events. The energy efficiency of the operation of SNN is calculated in comparison with that of a binary recurrent neural network (RNN) based on a hard sigmoid activation function [34] and ANN. The energy consumption of the neural network includes the consumption of synaptic operations and neuron operations, which is defined by the well-known energy analysis tool *KerasSpiking* for neural networks. In the synaptic operations, the output from the front layer is multiplied by the weight of each synapse. It should be noted that the overall energy consumption is not only affected by the abovementioned software operations but also by the hardware accelerators and its specifications. Neuromorphic

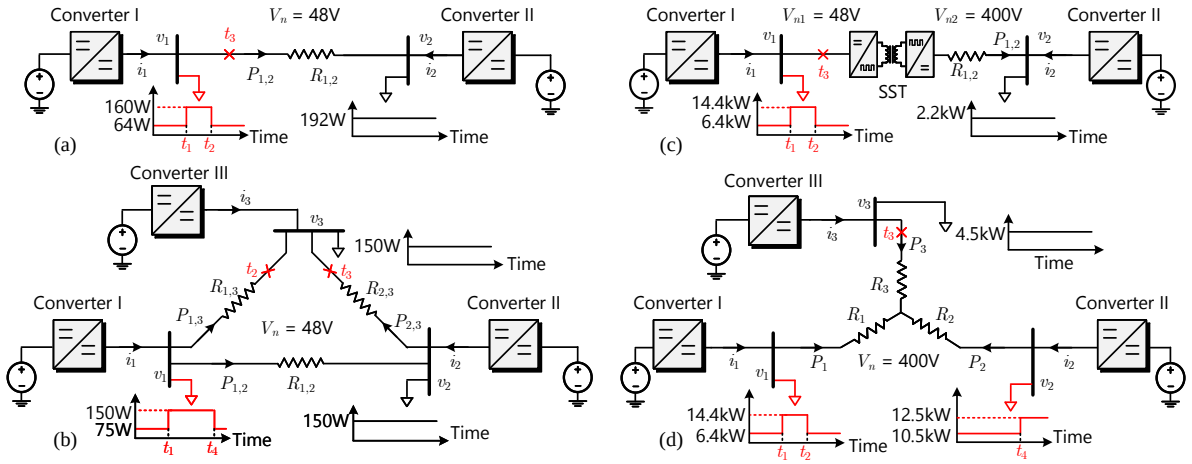

Fig. 4. Different topologies for verification: (a) Case I: Two-bus DC microgrid, (b) Case II: Three-bus DC microgrid in ring topology, (c) Case III: Two-bus DC microgrid with an intermediate solid-state transformer, (d) Case IV: Three-bus DC microgrid in star topology.

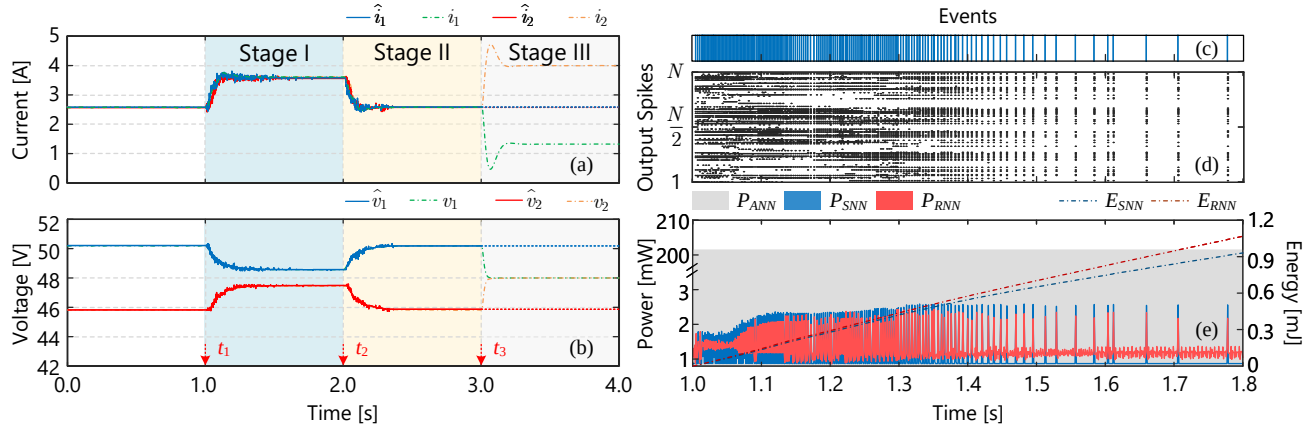

Fig. 5. Case I: (a) SNN-estimated and sampled currents, (b) SNN-estimated and sampled voltages, (c) captured events, (d) output spikes of SNN, and (e) comparison of SNN against ANN and RNN on power and accumulated energy consumption during a load transient.

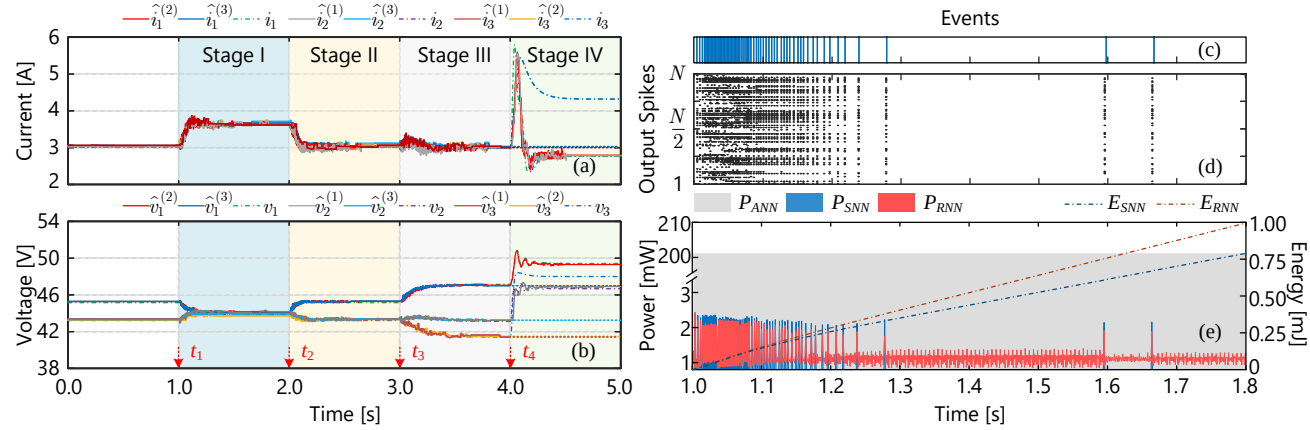

Fig. 6. Case II: (a) SNN-estimated and sampled currents, (b) SNN-estimated and sampled voltages, (c) captured events, (d) output spikes of SNN, and (e) comparison of SNN against ANN and RNN on power and accumulated energy consumption during a load transient.

computing with fully parallel crossbar array based processors with an inherent asynchronous address event representation (AER) architecture run only in the spiking domain for its inputs/outputs, that lowers the energy consumption. On the other hand, the clock based GPU processors for ANN only accept floating points as the data format, which increases the operations and computational power. Furthermore, SNN also uses the notion of leakage, which not only restrict its operation during events, but also limit the number of neurons in operation due to the Hebbian learning principle. However, ANN and binary-activated RNN are always in operation, which thereby increases the computation power. Hence, the energy efficiency in this paper only accounts the data format and asynchronous event based operation as the comparative aspects based on the benchmarking of SNN against ANN and binary-activated RNN.

The number of accumulations (ACC) and multiplication accumulations (MAC) in synaptic and neuron operations are

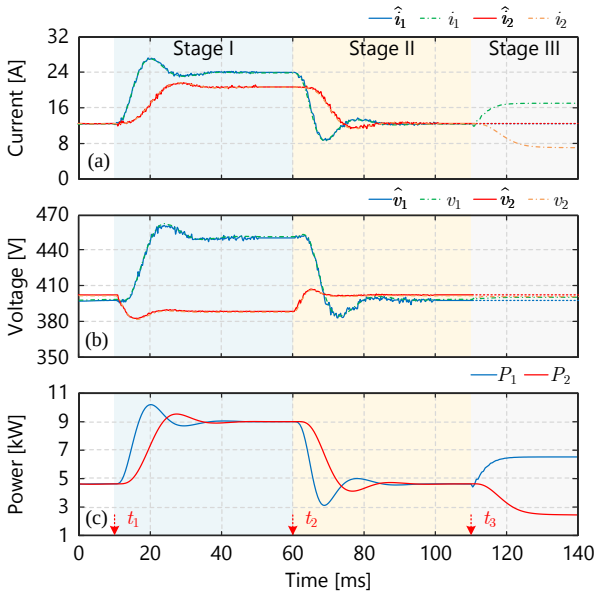

Fig. 7. Case III: (a) comparison of estimated and measured voltages, (b) currents, and (c) output powers.

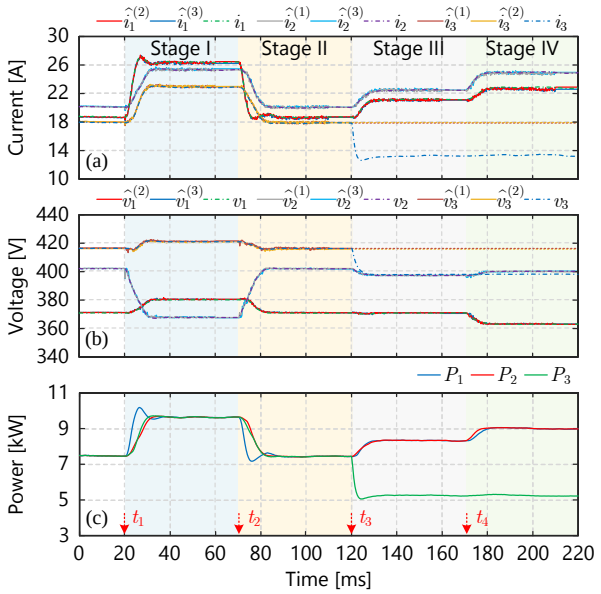

Fig. 8. Case IV: (a) comparison of estimated and measured voltages, (b) currents, and (c) output powers.

the fundamental energy consumption units that need to be considered for energy consumption [35]. The number of ACC and MAC for SNN, binary RNN and ANN is summarized in Table IV, where N_{ACC}^{ANN}, N_{MAC}^{ANN}, N_{ACC}^{RNN}, N_{MAC}^{RNN}, N_{ACC}^{SNN} and N_{MAC}^{SNN} are the number of ACC and MAC of the three said NNs. N_{in}, N_{out} are the number of neurons of the pre-synaptic and post-synaptic layer. N_{spk} in the number of spikes in SNN and binary RNN. Then the energy consumption can be estimated by (28a)-(28c).

$$E_{SNN}(t) = E_{ACC} \cdot N_{ACC}^{SNN}(t) + E_{MAC} \cdot N_{MAC}^{SNN}(t) \quad (28a)$$
$$E_{RNN}(t) = E_{ACC} \cdot N_{ACC}^{RNN}(t) + E_{MAC} \cdot N_{MAC}^{RNN}(t) \quad (28b)$$
$$E_{ANN}(t) = E_{ACC} \cdot N_{ACC}^{ANN}(t) + E_{MAC} \cdot N_{MAC}^{ANN}(t) \quad (28c)$$

where, E_{ACC} and E_{MAC} are the energy cost of single additions and multiplications respectively, which are respectively 0.1 pJ and 3.1 pJ [36]. The total energy consumption of SNN and binary RNN from the integration of their power consumptions are also plotted in Fig. 5(e). The final energy consumption is presented in Table V. With SNN staying *idle*/consuming no energy when there is no spike, the hard sigmoid activation function for binary-activated RNN may still generate spikes, which makes it less energy efficient than SNN. As for ANN, it is always on with real floating values, consequently consuming much more energy than SNN and binary RNN.

2) Case II: Three-bus DC microgrid in ring topology: As depicted in the three-bus system in Fig. 4(b), the same control objective in Case I is re-tested with more number of converters (with increased dimension of input data for training of SNN) and another topology. In Fig. 6(a) and (b), we compare the estimated currents and sampled currents, as well as the estimated voltages and sampled voltages. In that case, $\hat{i}_j^{(k)}$ represents the estimated i_j by converter k. With increase in load current at t_1, the current sharing control objective is successfully met, since the estimated currents from SNN comply with the dynamic variations incurred by the remote measurements.

At the instant t_3, the voltage and current dynamics of the three buses are influenced by a line outage. Since the SNN has been trained using data that includes line outage scenarios, it is capable of recognizing the line outage and estimating the voltage and current of other converters. Consequently, v_1, v_2, and v_3 are regulated to re-distribute the power flow in the network, while i_1, i_2, and i_3 remain equal, demonstrating the capability of NSC-based control to operate under line outage conditions. At the time t_4, Converter III becomes completely disconnected, leading to the secondary control loop in Converter III ceasing its operation, as indicated by the dotted line. However, Converter I and Converter II continue to function and maintain current sharing.

With the outage of converter III in stage IV, the estimated currents $\hat{i}_j^{(k)}$ and voltages $\hat{v}_j^{(k)}$ in Fig. 6(a) and (b) closely

TABLE IV
ACCs AND MACs IN SNN AND ANN.

	Synaptic operations	Neuron update	
N_{ACC}^{ANN}	0	$2N_{out}$	
N_{MAC}^{ANN}	$N_{in} \times N_{out}$	$3N_{out}$	
N_{ACC}^{RNN}	$N_{spk} \times N_{out}$	N_{out} (active)	0 (idle)
N_{MAC}^{RNN}	0	N_{out}	
N_{ACC}^{SNN}	$N_{spk} \times N_{out}$	$2N_{out}$ (active)	0 (idle)
N_{MAC}^{SNN}	0	N_{out}	

TABLE V
COMPARATIVE EVALUATION OF THE COMPUTATIONAL ENERGY.

	Case I ($t_{1\text{-}2}$)	Case II ($t_{1\text{-}2}$)
E_{SNN} (mJ)	0.921	0.788
E_{RNN} (mJ)	1.057	0.991
E_{ANN} (mJ)	168.47	168.47
$\sum_{t_1}^{t_2} N_{SNN}(t)$	8.795×10^6	3.585×10^6
$\sum_{t_1}^{t_2} N_{RNN}(t)$	14.894×10^6	12.342×10^6
$\sum_{t_1}^{t_2} N_{ANN}(t)$	1.065×10^8	1.065×10^8

match the corresponding measured values, demonstrating the effectiveness of NSC-based control in this case.

Events in Fig. 6(c) arise from the dynamic process, and the corresponding spikes in Fig. 6(d) are generated in tandem with these events. The calculation of power consumption by SNN, RNN, and ANN (Fig. 6(e)) follows the same procedure as in Case I. The total energy consumption of SNN and binary RNN is detailed in Table V.

3) Case III: Two-bus DC microgrid with an intermediate solid-state transformer (SST): In this scenario in Fig. 4 (c), all the values of Converter II are referred to the primary side of the SST as a reference for comparison with a control objective on power sharing between converters. In Fig. 7(a) and (b), we compare the estimated currents $\hat{i}_1$, $\hat{i}_2$ with the sampled currents i_1 and i_2, as well as the estimated voltages $\hat{v}_1$, $\hat{v}_2$ with the sampled voltages v_1 and v_2 during dynamic disturbances.

It can be seen in Fig. 7 that in both Stage I and Stage II, the estimated values $\hat{i}_2$ and $\hat{v}_2$ by Converter I closely match the sampled values i_2 and v_2 during dynamic processes, and vice versa. This results in equal power reference P_1 and P_2, which lead to real output powers P_1 and P_2 following their respective references to reach an equal steady state in Fig. 7(c). Beyond the governing limitations of TPC, we establish that NSC-based control is not limited by galvanic isolation along the transmission lines even at heterogeneous voltage levels.

4) Case IV: Three-bus DC microgrid in star topology: Considering a secondary control objective of power-sharing for a three-bus microgrid in a star topology in Fig. 4(d), when the load changes from 6.4 kW to 14.4 kW at Converter I at instant t_1, the power-sharing control is successfully met in Fig. 8 following the same principle as in Case III. At t_3, a line outage occurs, resulting in voltage regulation to redistribute the power flow. This leads to equal power references, as shown in Fig. 8(c). At t_4, Converter III is disconnected, causing the secondary control loop in Converter I to isolate, as indicated by the dotted line. However, Converters I and II still resort to power sharing.

Despite the isolation of Converter III in Stage IV, the estimated currents $\hat{i}_j$ and voltages $\hat{v}_j$ in Fig. 8(a) and (b) closely match the measured values, respectively. Consequently, P_1, P_2, and P_3 are equal, resulting in accurate estimation of remote measurements and signals using the proposed NSC-based coordination.

5) Case V: A modified IEEE 14-bus system: To better validate the scalability of the proposed method in a large system, tests are also conducted in a modified IEEE 14-bus system in Fig. 9, of which the network structure is identical to the standard IEEE 14-bus system but with scaled down DC interconnection network and sources.

The DERs are working at their maximum power point and only controlled by respective local controllers. The energy storage (ES) converters connected to batteries need to collaborate with each other to support the dynamic change of generated power from the DERs. The coordinated control objectives of secondary control are average voltage regulation and proportionate power sharing. The average voltage is regulated at a rated voltage of 400 V. The power between

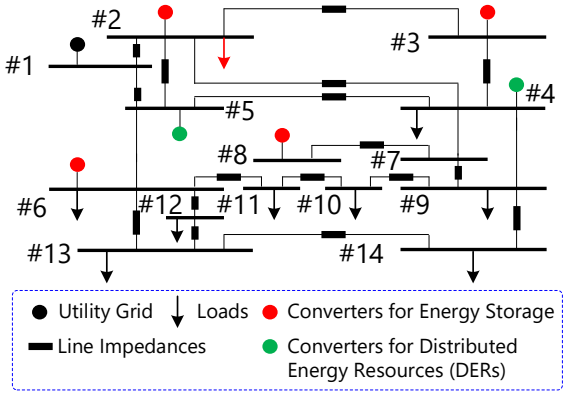

Fig. 9. Case V: Modified IEEE 14-bus DC system with energy storages and distributed energy resources (DERs).

the ES based converters is shared in a ratio of their respective state-of-charge (SOC) values, given by:

$$\gamma = \frac{P_{ES1}}{\Delta SOC_1} = \frac{P_{ES2}}{\Delta SOC_2} = \frac{P_{ES3}}{\Delta SOC_3} = \frac{P_{ES4}}{\Delta SOC_4} \tag{29}$$

such that

$$\Delta SOC_i = \begin{cases} SOC_{max} - SOC_i & \textit{when } \textbf{charging} \\ SOC_i - SOC_{min} & \textit{when } \textbf{discharging} \end{cases} \tag{30}$$

where, SOC_{max} and SOC_{min} are the maximum and minimum SOC limits of the batteries. The real-time SOC of each ES can be estimated by the following equation,

$$SOC(t) = SOC_{\text{initial}} - \frac{1}{C}\int i_{\text{bat}}(t)\mathrm{d}t \tag{31}$$

The current i_{bat} can be estimated by SNN, so the SOC of each ES can be known by the adjacent converters.

As we compare the estimated currents and voltages with the sampled values during dynamic disturbances, it can be seen in Fig. 10(a) and (b) that in Stage I, Stage II, and Stage III, the estimated values closely match the sampled values, which results in the power-sharing results shown in Fig. 10(c) and (d). They are aiming to be shared by the ratio of ΔSOC. As shown in Fig. 10(d), the ratio γ ($P_i/\Delta SOC$) is always equal, which indicates that the power P_1 - P_4 can always be shared according to the ratio of ΔSOC in (29).

B. Experiment results

A two-bus system illustrated in Fig. 11(b) has been employed for experimental validations, with the single-line diagram and other parametric details presented in Fig. 11(a). It comprises two DC/DC buck converters managing equal load current sharing. Dynamic events, such as load change and line outage are considered to check the efficacy of NSC under real-time conditions. The experimental parameters can be found in Table VI. The offline design of SNN and its corresponding parameters can be found in Appendix.

1) Load change: In Fig. 12(a), before the load change, currents i_1 and i_2 are equal. When the load transitions from 115 Ω to 75 Ωat t=0.2 s, a dynamic process is formalized leading to generation of output events, such that i_1 and i_2 maintain equal sharing. The voltage variables v_1 and v_2

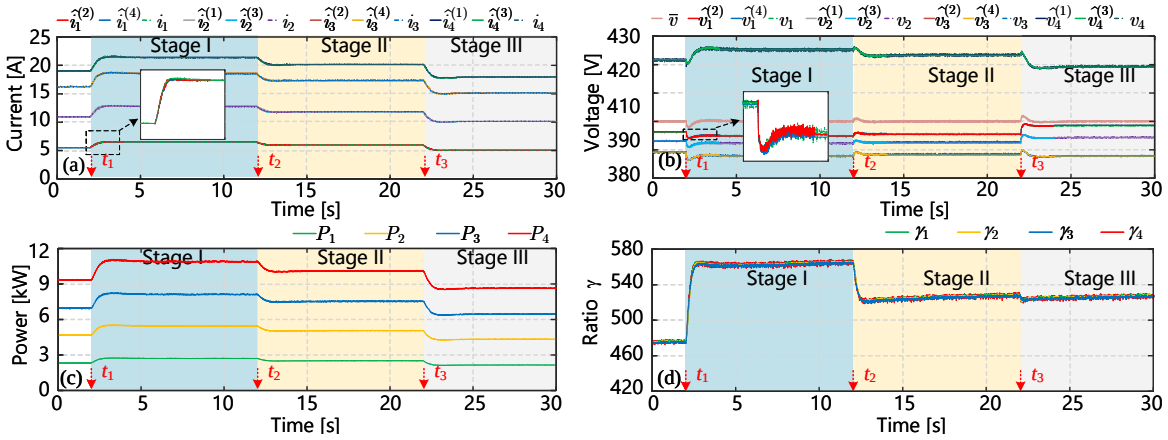

Fig. 10. Simulation results of the ES converters: (a) comparison of estimated currents and respective measured values, (b) comparison of estimated voltages and respective measured values, (c) output powers, and (d) γ (P_i/SOC ratio) of the ES converters.

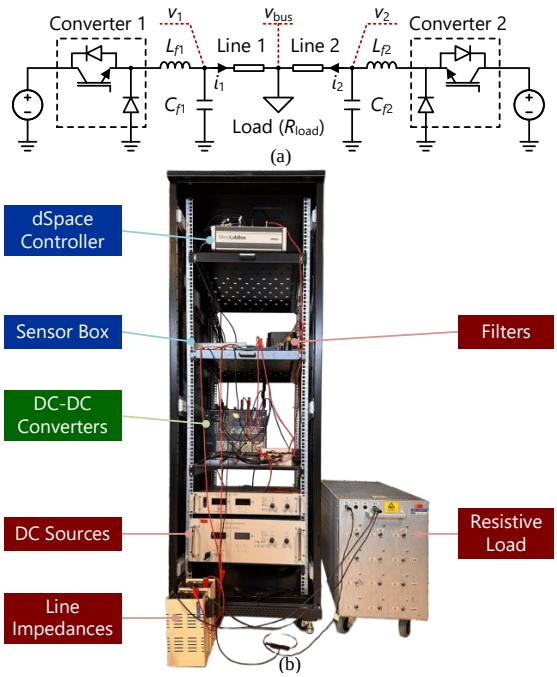

Fig. 11. Experimental setup: (a) Single-line diagram of the two DC/DC converters tied to each other via a common resistive load, (b) picture of the prototype.

TABLE VI
EXPERIMENTAL PARAMETERS.

Parameter	Symbol	Specification
Rated voltage	V_n	40 V
Rated power	P_1=P_2	50 W
Filter inductance	L_{f1}=L_{f2}	1.5 mH
Filter capacitance	C_{f1}=C_{f2}	700 μF
Line resistance	R_1, R_2	1.5 Ω, 3.6 Ω
Load resistance	R_{load}	115 Ω

experience a sag due to increased load, reaching two new steady states. In Fig. 12(b), i_2 is compared with its estimated value $\hat{i}_2$ by Converter I, ensuring accurate current sharing. During the dynamic process, events are generated, as depicted in Fig. 12(c), leading to corresponding spikes in the hidden layer of SNN, presented in Fig. 12(d).

Fig. 12(e) illustrates the load recovery from 75 Ω to 115 Ω, with both i_1 and i_2 decreasing and sharing the load equally after a dynamic process. Voltage variables v_1 and v_2 increase and return to their initial steady states. Control system variables for Converter I in this scenario are shown in Fig. 12(f) and (g). As seen in Fig. 12(f), the estimated value $\hat{i}_2$ accurately matches i_2, ensuring precise current sharing. During the dynamic process, events are generated in (g), and corresponding spikes in the hidden layer of SNN are generated in Fig. 12(h) synchronized with the events.

2) Line outage: In Fig. 13(a), before the line outage, i_1 and i_2 share an equal load. When Converter II is disconnected due to a line outage, both v_1 and v_{bus} sag due to power droop control. In Fig. 13(b), i_2 is compared with its estimated value $\hat{i}_2$ by Converter I, enabling Converter I to be aware of the states of Converter II. As Converter I operates in islanded mode, NSC based secondary control becomes inactive. During the dynamic process, events are generated, as depicted in (c), leading to corresponding spikes presented in Fig. 13(d).

Fig. 13(e) illustrates the scenario when Converter II is reconnected to the system at t = 2 s, with i_1 and i_2 returning to an equal state. This occurs because SNN is activated by local dynamics, allowing it to estimate i_2 again, as shown in Fig. 13(f). During the dynamic process, the SNN is activated by the events in Fig. 13(g), with corresponding spikes shown in Fig. 13(h).

V. CONCLUSIONS AND FUTURE SCOPE OF WORK

This paper explores a low-power neuromorphic inference based application for the first time in the realm of microgrids and power systems. We firstly leverage the deterministic features of information-theoretic learning using the highly energy-efficient spiking neural networks (SNNs) at each bus to estimate the remote measurements only using the unmodulated power flows as the information carrier to enable co-transfer of power and information. Secondly, we explore its application for the hierarchical control of microgrids as its application by leveraging the *publish-subscribe* architecture as a novel communication protocol for power electronic systems. Thirdly, since SNNs are trained using spikes based binary

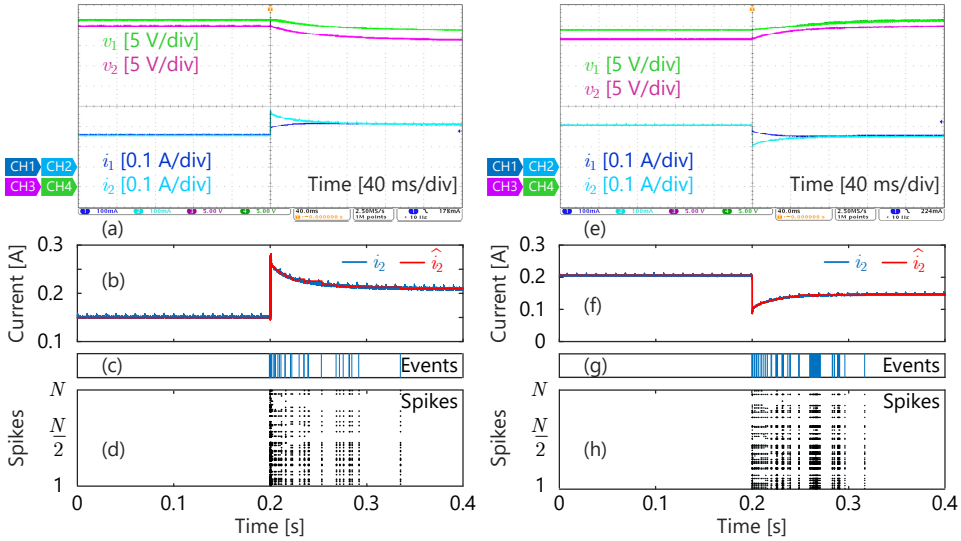

Fig. 12. Experimental results: (a) voltage and current when load increases, (b) current of Converter II and its estimated value by Converter I when load increases, (c) events when load increases, (d) the spikes of hidden layer in SNN, (e) voltage and current when load decreases, (f) current of Converter II and its estimated value by Converter I when load decreases, (g) events when load decreases, (h) the spikes of hidden layer in SNN.

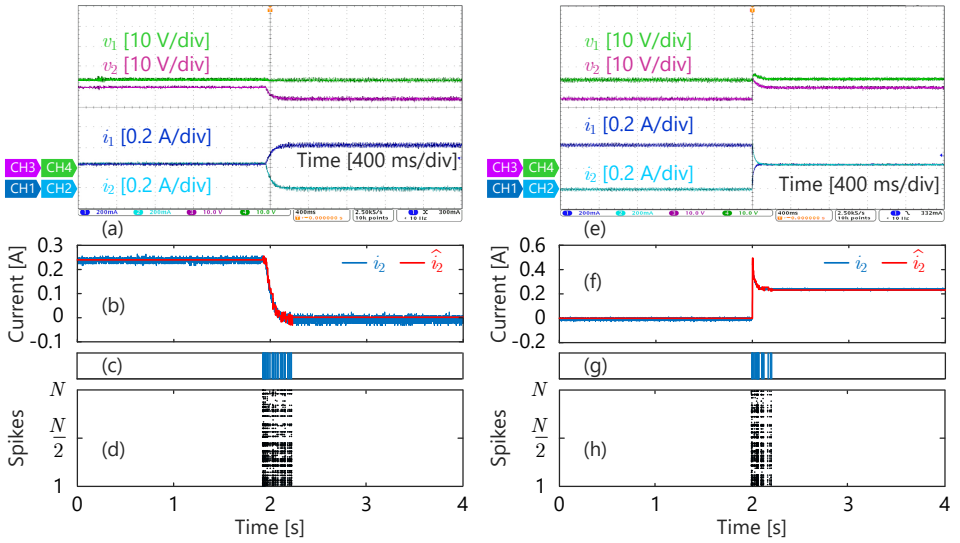

Fig. 13. Experimental results: (a) voltage and current when Converter II quits, (b) current of Converter II and its estimated value by Converter I when Converter II quits, (c) events when Converter II quits, (d) the spikes of hidden layer in SNN, (e) voltage and current when Converter II resumes operation, (f) current of Converter II and its estimated value by Converter I when Converter II resumes operation, (g) events when Converter II resumes operation, (h) the spikes of hidden layer in SNN.

data, we translate an event-driven sampling process to reflect on the most significant communicative signatures from the remote ends that are further converted to spikes for online training and inferences from SNNs, that is updated with every system transients. By doing so, we not only eliminate the communication infrastructure and their associated reliability and security concerns, but also clearly demonstrate the computational advantages, energy efficiency and feasibility behind using SNN over other data and computational-intensive neural networks. The proposed framework also eliminates the cyber layer vulnerabilities to restrict any exogenous path arrivals for the cyber attackers. Furthermore, it doesn't suffer from the inefficiency and scalability issues that other co-transfer technologies such as *Talkative Power Communication* will incur.

In the future, we plan to expand this philosophy to facilitate smarter integration or start-up of distributed energy sources and regional microgrids. The proposed scheme still needs to be validated on fully parallel memristor crossbar array circuits based processors with a specific focus on accuracy and versatility for different noise levels.

APPENDIX

A. SNN Parameters – Simulation Studies

Number of hidden layers = 2, Number of neurons in encoding and hidden layer = 256, Number of neurons in

decoding layer = 4, σ_{th}^{V} = 0.01, σ_{th}^{I} = 0.002, σ_{th}^{I} = 0.0039.

Dataset dimensions for the inputs and outputs in Case I and III : $\mathbb{D}_{in,800\times4} = \{\boldsymbol{v}_{i,800\times1},\ \boldsymbol{i}_{i,800\times1},\ \dot{\boldsymbol{v}}_{i,800\times1},\ \dot{\boldsymbol{i}}_{i,800\times1}\}$, $\mathbb{D}_{out,800\times2} = \{\hat{\boldsymbol{v}}_{j,800\times1}^{(i)},\ \hat{\boldsymbol{i}}_{j,800\times1}^{(i)},\}, \forall\ i,j \in \{1,2\}, i \neq j$.

Dataset dimensions for the inputs and outputs in Case II and IV : $\mathbb{D}_{in,800\times4} = \{\boldsymbol{v}_{i,800\times1},\ \boldsymbol{i}_{i,800\times1},\ \dot{\boldsymbol{v}}_{i,800\times1},\ \dot{\boldsymbol{i}}_{i,800\times1}\}$, $\mathbb{D}_{out,800\times4} = \{\hat{\boldsymbol{v}}_{j,800\times1}^{(i)},\ \hat{\boldsymbol{i}}_{j,800\times1}^{(i)},\ \hat{\boldsymbol{v}}_{k,800\times1}^{(i)},\ \hat{\boldsymbol{i}}_{k,800\times1}^{(i)}\}$, $\forall\ i,j,k \in \{1,2,3\}, i \neq j \neq k$.

B. SNN Parameters – Experimental Studies

Number of hidden layers = 2, Number of neurons in encoding and hidden layer = 64, Number of neurons in decoding layer = 4, σ_{th}^{V} = 0.41, σ_{th}^{I} = 0.0063, σ_{th}^{I} = 0.024.

Dataset dimensions for the inputs and outputs: $\mathbb{D}_{in,4000\times4} = \{\boldsymbol{v}_{i,4000\times1},\ \boldsymbol{i}_{i,4000\times1},\ \dot{\boldsymbol{v}}_{i,4000\times1},\ \dot{\boldsymbol{i}}_{i,4000\times1}\}$, $\mathbb{D}_{out,4000\times2} = \{\hat{\boldsymbol{v}}_{j,4000\times1}^{(i)},\ \hat{\boldsymbol{i}}_{j,800\times1}^{(i)},\}, \forall\ i,j \in \{1,2\}, i \neq j$.

REFERENCES

[1] S. Sahoo and S. Mishra, "A Distributed Finite-Time Secondary Average Voltage Regulation and Current Sharing Controller for DC Microgrids," *IEEE Trans. Smart Grid*, vol. 10, no. 1, pp. 282–292, Jan. 2019.

[2] J. M. Guerrero, M. Chandorkar, T.-L. Lee, and P. C. Loh, "Advanced Control Architectures for Intelligent Microgrids—Part I: Decentralized and Hierarchical Control," *IEEE Trans. Ind. Electron.*, vol. 60, no. 4, pp. 1254–1262, Apr. 2013.

[3] S. Sahoo and S. Mishra, "An Adaptive Event-Triggered Communication-based Distributed Secondary Control for DC Microgrids," *IEEE Trans. Smart Grid*, vol. 9, no. 6, pp. 6674–6683, Nov. 2018.

[4] E. Espina, R. Cárdenas-Dobson, J. W. Simpson-Porco, D. Sáez, and M. Kazerani, "A Consensus-Based Secondary Control Strategy for Hybrid AC/DC Microgrids with Experimental Validation," *IEEE Trans. Power Electron.*, vol. 36, no. 5, pp. 5971–5984, May. 2021.

[5] E. Espina, R. Cárdenas-Dobson, J. W. Simpson-Porco, M. Kazerani, and D. Sáez, "A Consensus-Based Distributed Secondary Control Optimization Strategy for Hybrid Microgrids," *IEEE Trans. Smart Grid*, vol. 14, no. 6, pp. 4242–4255, Nov. 2023.

[6] S. Sahoo and F. Blaabjerg, "A model-free predictive controller for networked microgrids with random communication delays," in *2021 IEEE Applied Power Electronics Conference and Exposition (APEC)*, 2021, pp. 2667–2672.

[7] M. Dong, L. Li, Y. Nie, D. Song, and J. Yang, "Stability Analysis of a Novel Distributed Secondary Control Considering Communication Delay in DC Microgrids," *IEEE Trans. Smart Grid*, vol. 10, no. 6, pp. 6690–6700, Nov. 2019.

[8] S. Sahoo, S. Mishra, J. C.-H. Peng, and T. Dragičević, "A Stealth Cyber-Attack Detection Strategy for DC Microgrids," *IEEE Trans. Power Electron.*, vol. 34, no. 8, pp. 8162–8174, Aug. 2019.

[9] X. Wu, S. Deng, W. Yuan, and S. Mei, "A Robust Distributed Secondary Control of Microgrids Considering Communication Failures," in *Proc. 2022 ICPET*, Beijing, China, Jul. 2022, pp. 395–400.

[10] M. Angjelichinoski, Č. Stefanović, P. Popovski, H. Liu, P. C. Loh, and F. Blaabjerg, "Multiuser Communication Through Power Talk in DC Microgrids," *IEEE J. Sel. Areas Commun.*, vol. 34, no. 7, pp. 2006–2021, Jul. 2016.

[11] X. He, R. Wang, J. Wu, and W. Li, "Nature of Power Electronics and Integration of Power Conversion with Communication for Talkative Power," *Nat. Commun.*, vol. 11, no. 1, p. 2479, May. 2020.

[12] Y. Zhu, J. Wu, R. Wang, Z. Lin, and X. He, "Embedding Power Line Communication in Photovoltaic Optimizer by Modulating Data in Power Control Loop," *IEEE Trans. Ind. Electron.*, vol. 66, no. 5, pp. 3948–3958, May. 2019.

[13] J. Chen, K. Liu, J. Wu, R. Wang, W. Weng, and X. He, "Simultaneous Power and Data Transmission Using Combined Three Degrees of Freedom Modulation Strategy in DC-DC Converters," *IEEE Trans. Power Electron.*, vol. 38, no. 3, pp. 3191–3200, Mar. 2022.

[14] P. A. Hoeher, J. M. Placzek, M. Hott, and M. Liserre, "Networking Aspects based on the Talkative Power Concept for DC Microgrid Systems," in *Proc. 2022 IEEE PEDG*, Kiel, Germany, Jun. 2022, pp. 1–6.

[15] Y. Leng, D. Yu, K. Han, S. S. Yu, and Y. Hu, "OFDM-based Intrinsically Safe Power and Signal Synchronous Transmission for CC-PT-Controlled Buck Converters," *IEEE Trans. Power Electron.*, vol. 37, no. 9, pp. 10 319–10 331, Sep, 2022.

[16] D. Gündüz, Z. Qin, I. E. Aguerri, H. S. Dhillon, Z. Yang, A. Yener, K. K. Wong, and C.-B. Chae, "Beyond Transmitting Bits: Context, Semantics, and Task-oriented Communications," *IEEE J. Sel. Areas Commun.*, vol. 41, no. 1, pp. 5–41, Jan. 2023.

[17] Z. Ma, Z. Wang, Y. Guo, Y. Yuan, and H. Chen, "Nonlinear Multiple Models Adaptive Secondary Voltage Control of Microgrids," *IEEE Trans. Smart Grid*, vol. 12, no. 1, pp. 227–238, Jan. 2021.

[18] H. Jang, O. Simeone, B. Gardner, and A. Gruning, "An Introduction to Probabilistic Spiking Neural Networks: Probabilistic Models, Learning Rules, and Applications," *IEEE Signal Process. Mag.*, vol. 36, no. 6, pp. 64–77, Nov. 2019.

[19] P. Popovski, *Wireless Connectivity: An Intuitive and Fundamental Guide*. John Wiley & Sons, 2020.

[20] K. Roy, A. Jaiswal, and P. Panda, "Towards Spike-based Machine Intelligence with Neuromorphic Computing," *Nature*, vol. 575, no. 7784, pp. 607–617, Nov. 2019.

[21] L. Deng, Y. Wu, X. Hu, L. Liang, Y. Ding, G. Li, G. Zhao, P. Li, and Y. Xie, "Rethinking the Performance Comparison Between SNNS and ANNS," *Neural Networks*, vol. 121, pp. 294–307, Jan. 2020.

[22] S. Nitzsche, B. Pachideh, M. Neher, M. Kreutzer, N. Link, L. Theurer, and J. Becker, "Comparison of Artificial and Spiking Neural Networks for Ambient-Assisted Living," in *Proc. 2022 IEEE SSI*, Grenoble, France, Apr. 2022, pp. 1–6.

[23] R. Vaila, J. Chiasson, and V. Saxena, "A Deep Unsupervised Feature Learning Spiking Neural Network with Binarized Classification Layers for the EMNIST Classification," *IEEE Trans. Emerging Topics Comput. Intell.*, vol. 6, no. 1, pp. 124–135, Feb. 2022.

[24] J. Chen, N. Skatchkovsky, and O. Simeone, "Neuromorphic Wireless Cognition: Event-driven Semantic Communications for Remote Inference," *IEEE Trans. Cogn. Commun.*, Jan. 2023.

[25] K. Gupta, S. Sahoo, and B. K. Panigrahi, "Delay-aware semantic sampling in power electronic systems," *IEEE Transactions on Smart Grid*, 2023, early access.

[26] K. Gupta, S. Sahoo, and B. K. Panigrahi, "A monolithic cybersecurity architecture for power electronic systems," *IEEE Transactions on Smart Grid*, 2024, early access.

[27] A. Bidram, A. Davoudi, F. L. Lewis, and J. M. Guerrero, "Distributed Cooperative Secondary Control of Microgrids Using Feedback Linearization," *IEEE Trans. Power Syst.*, vol. 28, no. 3, pp. 3462–3470, Aug. 2013.

[28] S. Rath, L. D. Nguyen, S. Sahoo, and P. Popovski, "Self-Healing Secure Blockchain Framework in Microgrids," *IEEE Trans. Smart Grid*, vol. 14, no. 6, pp. 4729–4740, 2023.

[29] M. Rozenberg, O. Schneegans, and P. Stoliar, "An ultra-compact leaky-integrate-and-fire model for building spiking neural networks," *Scientific reports*, vol. 9, no. 1, p. 11123, 2019.

[30] L. Ding, Q.-L. Han, X. Ge, and X.-M. Zhang, "An Overview of Recent Advances in Event-Triggered Consensus of Multiagent Systems," *IEEE Trans. Cybern.*, vol. 48, no. 4, pp. 1110–1123, 2018.

[31] S. Sahoo, Y. Yang, and F. Blaabjerg, "Resilient synchronization strategy for ac microgrids under cyber attacks," *IEEE Transactions on Power Electronics*, vol. 36, no. 1, pp. 73–77, 2021.

[32] V. Saranirad, S. Dora, T. M. McGinnity, and D. Coyle, "Assembly-based stdp: A new learning rule for spiking neural networks inspired by biological assemblies," in *2022 International Joint Conference on Neural Networks (IJCNN)*. IEEE, 2022, pp. 1–7.

[33] A. Payeur, J. Guerguiev, F. Zenke, B. A. Richards, and R. Naud, "Burst-dependent synaptic plasticity can coordinate learning in hierarchical circuits," *Nature neuroscience*, vol. 24, no. 7, pp. 1010–1019, 2021.

[34] M. Courbariaux, Y. Bengio, and J.-P. David, "Binaryconnect: Training deep neural networks with binary weights during propagations," in *Advances in Neural Information Processing Systems*, C. Cortes, N. Lawrence, D. Lee, M. Sugiyama, and R. Garnett, Eds., vol. 28. Curran Associates, Inc., 2015.

[35] E. Lemaire, L. Cordone, A. Castagnetti, P.-E. Novac, J. Courtois, and B. Miramond, "An Analytical Estimation of Spiking Neural Networks Energy Efficiency," in *Proc. International Conference on Neural Information Processing*. Springer, 2022, pp. 574–587.

[36] N. P. Jouppi and et. al., "Ten Lessons From Three Generations Shaped Google's TPUv4i : Industrial Product," in *Proc. 2021 ACM/IEEE 48th Annual International Symposium on Computer Architecture (ISCA)*, 2021, pp. 1–14.